Tang T. & Huang L. (2021). Mie particle assembly by a converging ultrasound field and acoustic interaction forces. *Applied Acoustics*.
DOI: 10.1016/j.apacoust.2021.108123

# Mie particle assembly by a converging ultrasound field and acoustic interaction forces

Tianquan Tang[a, b,*], Lixi Huang[a,b]

[a]Department of Mechanical Engineering, The University of Hong Kong, Pokfulam, Hong Kong SAR, China

[b]Lab for Aerodynamics and Acoustics, HKU Zhejiang Institute of Research and Innovation, 1623 Dayuan Road, Lin An District, Hangzhou, China

[*]Corresponding author: tianquan@connect.hku.hk

## Abstract

There has been growing interest in exerting radiation forces to trap and cluster randomly distributed cells in body fluid, micro-particles in water, or microorganisms in fluid-like culture media. Acoustic standing waves are extensively utilized as a patterning tool to assemble particles at nodes or anti-nodes but, for frequencies above megahertz, the nodal distances become too small for particle separation. We study a mechanism to propel particles towards one central space by creating a converging wave field without significant reflections. This is achieved by strong decay of the main ultrasound beam by multiple scattering. When two opposing traveling waves are suitably decayed towards their meeting point, a converging wave field is created for particle

assembly via radiation forces. This paper describes the theoretical prediction model based on the translation addition theorem and the partial-wave expansion method. The predicted acoustic pressure fields are compared with full numerical simulations for a limited number of particles, and the attenuation coefficient is validated by the existing experimental data. The results demonstrate that the converging wave field is formed, and the acoustic radiation force vectors in a bulk acoustic wave (BAW) device are directed towards the central space for meaningful clustering of micro-particles from their host fluid.

**Keywords:**

Mie particle assembly, Acoustic interaction forces, Acoustic energy dissipation, Bulk acoustic wave (BAW)

# 1. Introduction

In recent years, operations such as trapping [1][2][3][4][5], levitating [6][7][8][9], separating [2][10][11], printing [12], and clustering [13] the objects with different sizes in the air [6][7][8][14], water [1][15] and other fluid-like media [2][4][16] using acoustic radiation forces are becoming increasingly popular with a range of lab-on-a-chip applications.

Fundamentally, the propagation of an acoustic wave results in acoustic radiation forces on particles and the acoustic streaming of fluids. These are second-order effects, caused by nonlinearities in the governing physics. Lord Rayleigh laid the foundation of acoustic streaming [17] and the acoustic radiation force on a plane obstacle due to a propagating wave [18]. Modern understanding of acoustic radiation forces began with King [19], who developed theoretical formulas for the force on a rigid sphere in an inviscid fluid exerted by in-plane standing or traveling waves. It was extended to solve the problems with compressible and elastic boundaries [20][21]. Gor'kov generalized these results to arbitrary acoustic fields, showing that the time-averaged acoustic radiation force on a microparticle can be described by a potential [22] whose gradient is the exerted force. However, in the case of manipulating or levitating countable Mie particles, i.e., particles with diameters comparable with the wavelength, the scattering potential from the wave reflection by the particle itself and the rescattering potentials from other particles [23] become significant. The countable number of particles allows us to use Newton's law to describe the movement of each particle in the Lagrangian framework.

In order to analyze and evaluate the radiation forces acting upon any specific probe particle surrounded by multiple reciprocal particles, it is convenient to use the partial-wave expansion [24] to formulate the acoustic velocity potential fields. In this way, the scattering or rescattering fields can be obtained precisely with the help of a translation addition theorem [25]. This mathematical combination for the multi-particle problem has been applied widely [23][26]. In addition, as the acoustic forces acting upon a single particle can be directly evaluated by integrating the radiation stress tensor produced by the incident and scattered waves over the probe particle surface [27][28], a series expression for the radiation force components for a single particle within the host fluid [29] or a specific probe particle within the multiple particles environment [23] is obtained in the Cartesian coordinates. Moreover, as the incident wave with arbitrary wavefront can be formulated by partial-wave expansion [30], the expansion can combine with the series expression for the acoustic radiation forces. As a result, the radiation forces with arbitrary incident wavefront can be evaluated.

With the help of acoustic radiation forces, many promising applications of clustering multiple particles have been analyzed in recent years. The bulk acoustic wave (BAW) device [1] with two orthogonal standing waves was frequently used to rearrange the patterns of small particles [2][4][16][31]. Typically, scaffold patterning can be achieved by standing waves as the acoustic energy landscape forces the particles into potential wells [22]. In Owens's research [2], based on the principle that the Rayleigh particles are assembled at the nodes or anti-nodes decided by their natural properties of acoustic contrast factor, the negative acoustic contrast particles could be

separated from the positive ones. Similarly, Atehortua [11] presented a method utilizing the radiation forces acting upon the water droplets of the water/oil emulsion to make the small water droplets coalesce into bigger droplets in the nodes and realized the separation of crude oil from water. A comprehensive theoretical and experimental investigation of the scaffold patterning by standing waves for Rayleigh and Mie particles was conducted by Silva [31].

The effects of dissipation and absorption of acoustic energy hardly affect the principle of particle assembling when the number and the size of the particles are relatively small. However, when the volume concentration of the suspension becomes high, such as the case of randomly distributed cells in body fluid, the micro-particle in wastewater, and the small droplets in the clouds, energy dissipation by scattering plays an essential role in formulating the radiation force vectors.

Normally, a theory for energy dissipation by viscosity, heat transfer, and acoustic scattering effects begins with a single particle immersed in the host fluid, which is then extended to the environment of multiple particles under the premise that the overall energy dissipation satisfies the superposition principle by summing up the energy dissipation derived from the single-particle environment [32][33][34][35]. Many experiments in terms of Rayleigh particles [34][36][37 ] and Mie particles [35][38][39] with different volume concentrations had been conducted to validate the superposition principle. Although the attenuation coefficient calculated by the superposition principle agreed well with experiments for low volume-concentration suspensions, as the mutual effects among the particles are negligible, deviations become considerable for high volume concentrations. Therefore, the mutual effects should be considered by deriving the

potential field from the multi-particle environment. In this way, the acoustic energy conservation is used to describe the relationship between the dissipation and the acoustic velocity potential [40], and then the dissipation can also be formulated by partial-wave expansion consistently.

As the wave energy dissipation by scattering from the multiple Mie particles becomes significant, the familiar standing wave pattern is replaced by a traveling wave with decaying amplitudes. Since the radiation forces roughly point to the minima of the potential [22], particles should be assembled in the central space rather than the scaffolding nodes or anti-nodes in a standing wave inside the BAW device. As a result, droplets will coalesce to form rainfall, novel contactless 3D printing techniques, and material selection in the refining industry may benefit from this new particle assembly mechanism.

The rest of the paper is organized as follows. In Sec. 2, we present a series expression for the acoustic velocity potential sourced by the incident waves with arbitrary wavefront, which considers the mutual effects among different particles with the help of the addition theorem. To be physically consistent, we divide the whole potential field into three parts, the innermost domain, the outermost domain, and the middle layer. The effects of wave dissipation are evaluated using the potential of the outermost domain. The radiation forces are obtained by the surface integral of the probe particle using the potential of the innermost domain. In Sec. 3.1, the theoretical predictions of the pressure field are compared with full numerical simulation, and the attenuation coefficient is validated by the available experimental data. We introduce the geometric parameters of the computational domain and the operating parameters for computations used in the BAW

device in Sec. 3.2. The distribution of force vectors with scattering effects is analyzed and compared with numerical simulation in Sec. 3.3. A summary is made in Sec. 4.

## 2. Theoretical analysis

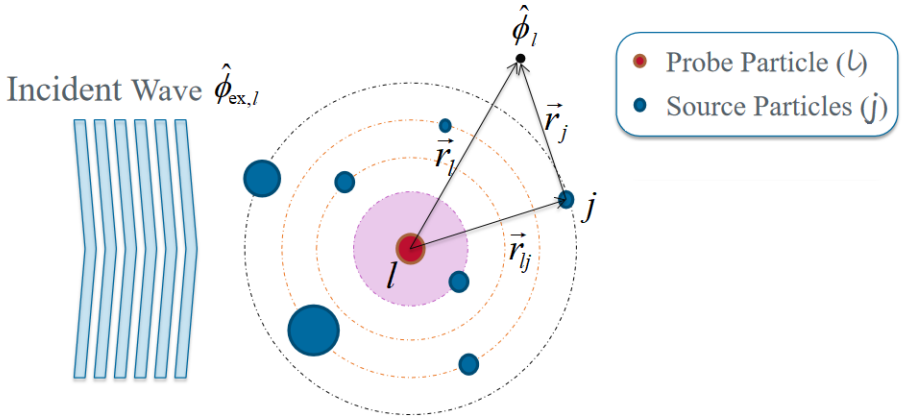


Fig. 1 Geometric description of multiple particles in a suspension and their relative positions used in the translation addition theorem.

Figure 1 shows the multi-particle system where a time-harmonic (with angular frequency $\omega$) external incident wave with arbitrary wavefront interacts with a set of spherical particles. The particles have radii $a_i (i = 1, 2, ...)$, with density $\rho_i$ and speed of sound $c_i$. The center of each particle defines a coordinate system denoted by $O_i$. We choose one of the particles as the object for the following derivations, which is referred to as probe particle (with index $i = l$). The position of any field point relative to the center of the probe particle is $\vec{r}_l$. All other particles are referred to as the source particles for scattering waves with index $j \neq l$, and the field points are located in the source particle coordinates $O_j$ as $\vec{r}_j$, while the source particles of the index $j$ are located by the probe coordinate system $O_l$ as $\vec{r}_{lj}$, with $\vec{r}_{lj} = \vec{r}_l - \vec{r}_j$. For simplicity, we consider an inviscid fluid, which satisfies the viscous thickness requirement [17], with density $\rho_0$ and speed of sound $c_0$, and particles are made by fluids or fluid-like homogeneous

materials for which shear waves can be ignored. Even when the particles are not fluid-like materials, fluid-like boundary conditions (continuity of the pressure and the radial component of fluid velocity) are sufficient to provide accurate numerical results [41][42]. In this case, any velocity potential function $\hat{\phi}(\vec{r}_i)$ (also denoted as $\hat{\phi}_i$) at a specific position $\vec{r}_i$ with respect to the system $O_i(i=1,2,...)$ satisfies the Helmholtz equation

$$\left(\nabla^2 + k^2\right)\hat{\phi}_i = 0, \tag{1}$$

where $\nabla^2$ is Laplace Operator, the hat symbol $\hat{}$ represents the complex amplitude, and $k$ is the wavenumber for the fluid. The velocity potential function with respect to the probe system $O_l$ is contributed by the external incident wave $\hat{\phi}_{\text{ex}}(\vec{r}_l)$ (denoted as $\hat{\phi}_{\text{ex},l}$), the scattering wave of the probe particle $\hat{\phi}_{\text{sc}}(\vec{r}_l)$ (denoted as $\hat{\phi}_{\text{sc},l}$), and the rescattering wave of all source particles $\hat{\phi}_{\text{rsc}}(\vec{r}_l)$ (denoted as $\hat{\phi}_{\text{rsc},l}$),

$$\hat{\phi}_l = \hat{\phi}_{\text{ex},l} + \underbrace{\hat{\phi}_{\text{sc},l} + \hat{\phi}_{\text{rsc},l}}_{\hat{\phi}_{\text{tsc},l}}, \tag{2}$$

while the sum of the two scattering potentials is called the total scattering potential function $\hat{\phi}_{\text{tsc}}(\vec{r}_l)$ (denoted as $\hat{\phi}_{\text{tsc},l}$).

Physically, in the near-field of the probe particle, a combination of the first and third terms on the right-hand side of Eq. (2) can be regarded as an effective incident velocity potential, and the second term as the scattering velocity potential. By contrast, in the far-field region, a combination of the second and third terms constitutes the total (effective) scattering velocity potential, while the first term remains as the external velocity potential.

## 2.1. Multiple scattering and the potential fIelds

To utilize the wave expansion technique in the spherical coordinate system, the potential of the external incident wave can be described by spherical partial-wave series [24] for an arbitrary probe particle coordinate system $O_i$ as

$$\hat{\phi}_{\mathrm{ex},i} = \sum_{n,m} a_{nm,i} J_{n,i}^{m}, \tag{3}$$

where $\sum_{n,m} \equiv \sum_{n=0}^{+\infty} \sum_{m=-n}^{+n}$ and $J_{n,i}^{m} \equiv j_n\left(kr_i\right) Y_n^m\left(\theta_i, \varphi_i\right)$. $j_n\left(kr_i\right)$ is the spherical Bessel function of order $n$ at the position $r_i$, and $Y_n^m\left(\theta_i, \varphi_i\right)$ is the spherical harmonic of $n$ th-order and $m$ th-degree at the angular position $\left(\theta_i, \varphi_i\right)$. $\theta_i$ and $\varphi_i$ are the polar and azimuthal angles of a spherical coordinate system $O_i$, respectively. Notably, the coefficients $a_{nm,i}$ are defined as the beam-shape coefficients of the spherical coordinate system $O_i$, which depend on the type of external wave considered (plane, cylindrical, spherical waves, or other beams, etc.). It can be regarded as a series of coefficients to approach an arbitrary wavefront of the external wave. A method based on the partial-wave expansion to formulate the beam-shape coefficients of the probe system $a_{nm,l}$ can be found in [30].

The information among different coordinate systems can be mutually expressed using the translation addition theorem [25]. The beam-shape coefficients of different coordinate systems $a_{nm,j}$ can be expressed by the beam-shape coefficients of the coordinate system of probe particle $a_{nm,l}$ as

$$a_{nm,j} = \sum_{\nu,\mu} a_{\nu\mu,l} S_{\nu,n}^{\mu,m\,(1)}\left(\vec{r}_{lj}\right), \quad j = 1,2,\cdots \text{but } j \neq l \tag{4}$$

where $S_{\nu,n}^{\mu,m\,(1)}\left(\vec{r}_{lj}\right)$ is the separation transform matrix of the first kind, which is used to transform the values of the beam-shape coefficients among different coordinate systems. Based on Eq. (4), if the beam-shape coefficients of the probe system $a_{nm,l}$ and the relative position vector $\vec{r}_{lj}$ are determined, the beam-shape coefficients of any source system $a_{nm,j}$ can be calculated.

As mentioned before, each particle contributes to the total scattering field, thereby making the problem much more complicated. The velocity potential function for the scattered field by one of the coordinate systems $O_i$ can be described as

$$\hat{\phi}_{\mathrm{sc},i} = \sum_{n,m} s_{nm,i} H_{n,i}^{m}, \quad i = 1,2,..., \tag{5}$$

where the scattering coefficients, $s_{nm,i}$, describe the scattering effects from multi-particle under the system $O_i$. A combining function $H_{n,i}^{m} \equiv h_n\left(kr_i\right) Y_n^m\left(\theta_i, \varphi_i\right)$. $h_n\left(kr_i\right)$ is the Hankel function of the first kind at the position $r_i$. Therefore, the total scattering potential function $\phi_{\mathrm{tsc}}$ can be found by summing contributions from all the scattering fields of the particles

$$\hat{\phi}_{\mathrm{tsc}} = \sum_{i=1,2,...} \hat{\phi}_{\mathrm{sc},i} = \sum_{i=1,2,...} \sum_{n,m} s_{nm,i} H_{n,i}^{m}. \tag{6}$$

Once all the scattering coefficients, $s_{nm,i}$, are determined, the total scattering potential field and the whole potential field are obtained. In order to solve the scattering coefficients, we need to use the boundary conditions between the particles and the host fluid.

The calculation of Eq. (6) requires all data from different coordinate systems for the coefficients $s_{nm,i}$ and the function $H_{n,i}^{m}$, which is unnecessary and difficult to handle. To simplify, the

information of all coordinate systems can be put into the coordinate system of probe particle $O_l$ by the translation addition theorem.

Mathematically, the addition theorem has different translation expressions depending on the relations between the distance of a particle to the center of the probe particle $|\vec{r}_l|$ and the distance of the center of the probe particle to the center of the translating source particle $|\vec{r}_{lj}|$ [25]. We divide the whole computational domain into three parts, as shown in Fig. 2.

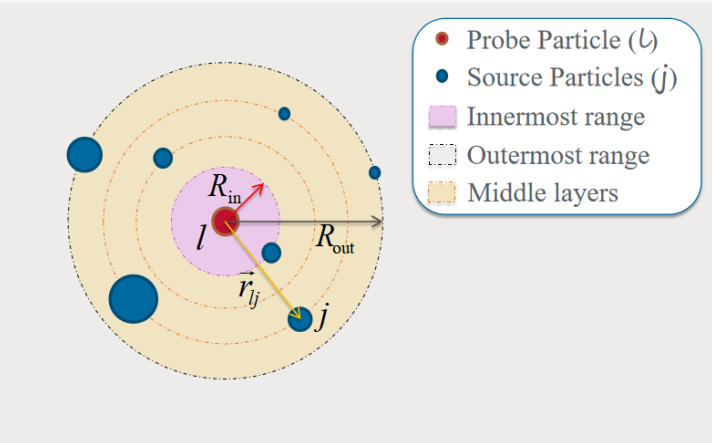


Fig. 2 Definition of the innermost domain, the outermost domain, and the middle layers in the translation addition theorem.

For the innermost domain (cf Fig. 2), where all source particles distribute outside of this region with respect to the system $O_l$ (i.e., $|\vec{r}_l| \le R_{\text{in}}$), the total effects of all scattering fields from all particles Eq. (6) can be rewritten as

$$\hat{\phi}_{\mathrm{tsc},l} = \sum_{n,m} s_{nm,l} H_{n,l}^{m} + \sum_{n,m} \left( \sum_{j\neq l} \sum_{\nu,\mu} s_{\nu\mu,j} S_{\nu,n}^{\mu,m(2)} \left( \vec{r}_{jl} \right) \right) J_{n,l}^{m} \tag{7}$$
$$= \underbrace{\sum_{n,m} s_{nm,l} H_{n,l}^{m}}_{\hat{\phi}_{\mathrm{sc},l}} + \underbrace{\sum_{n,m} rs_{nm,l}^{(\mathrm{in})} J_{n,l}^{m}}_{\hat{\phi}_{\mathrm{rsc},l}},$$

where $\sum_{j\neq l} \equiv \sum_{j=1,2,3...\&\, j\neq l}$, $S_{\nu,n}^{\mu,m(2)} \left( \vec{r}_{jl} \right)$ means the separation transform matrix of the second kind, which is used to transform the values of the scattering coefficients among different coordinate systems. $rs_{nm,l}^{(\mathrm{in})} \equiv \sum_{j\neq l} \sum_{\nu,\mu} s_{\nu\mu,j} S_{\nu,n}^{\mu,m(2)} \left( \vec{r}_{jl} \right)$ are the rescattering coefficients of the innermost domain with respect to the coordinate system $O_l$, describing the rescattering contributions from all source particles.

The rescattering coefficients of the innermost domain $rs_{nm,l}^{(\mathrm{in})}$ are directly decided by the scattering coefficients $s_{nm,i}$. It implies that if the scattering coefficients $s_{nm,i}$ are determined, the total scattering field from Eq. (7) can be calculated. It can be seen that the total number of unknown variables of the scattering coefficients $s_{nm,i}$ is $(M+1)^2 \times N$, where $M$ and $N$ are, respectively, the truncation number and the number of particles. Therefore, to determine the scattering coefficients $s_{nm,i}$, a set of $(M+1)^2 \times N$ equations is required, which is derived in Appendix I.

In the innermost domain, Eqs (2), (3), and (7) may be combined to show the potential function $\hat{\phi}_l$ with respect to $O_l$ as follows

$$\hat{\phi}_l = \sum_{n,m} \left( a_{nm,l} + rs_{nm,l}^{(\mathrm{in})} \right) J_{n,l}^{m} + \sum_{n,m} s_{nm,l} H_{n,l}^{m} \tag{8}$$
$$= \sum_{n,m} b_{nm,l} J_{n,l}^{m} + \sum_{n,m} b_{nm,l} s_{n,l} H_{n,l}^{m}.$$

The effective beam-shape coefficients $b_{nm,i}$ and the scalar scattering coefficients $s_{n,i}$ are

defined in Appendix I. It is worth noting that, for the innermost domain, the velocity potential function $\hat{\phi}_l$ can be physically separated into two parts, namely, the effective incident potential and the effective scattering potential. In this case, the rescattering waves from all source particles can be thought of as other external waves considered in the first part, and the effective scattering wave of the probe particle depends on not only the external incident wave, but also these rescattering external waves. In this sense, the multi-particle system becomes a single-particle system with respect to the innermost domain. Similar formulas to describe the innermost domain were also presented in [23].

In the outermost domain (seeing Fig. 2), where all source particles are distributed inside the region with respect to the system $O_l$ (i.e., $|\vec{r}_l| \geq R_{\text{out}}$), the total scattering fields Eq. (6) can be rewritten as

$$\begin{aligned}\hat{\phi}_{\text{tsc},l} &= \sum_{n,m} s_{nm,l} H_{n,l}^m + \sum_{n,m}\left(\sum_{j\neq l}\sum_{\nu,\mu} s_{\nu\mu,j} S_{\nu,n}^{\mu,m(1)}\left(\vec{r}_{jl}\right)\right) H_{n,l}^m \\ &= \underbrace{\sum_{n,m} s_{nm,l} H_{n,l}^m}_{\hat{\phi}_{\text{sc},l}} + \underbrace{\sum_{n,m} rs_{nm,l}^{(\text{out})} H_{n,l}^m}_{\hat{\phi}_{\text{rsc},l}},\end{aligned} \tag{9}$$

where $rs_{nm,l}^{(\text{out})} \equiv \sum_{j\neq l}\sum_{\nu,\mu} s_{\nu\mu,j} S_{\nu,n}^{\mu,m(1)}\left(\vec{r}_{jl}\right)$ are the rescattering coefficients of the outermost domain, which describe the rescattering contributions from all source particles.

Similarly, inserting Eq. (3) and Eq. (9) into Eq. (2) yields the potential field of the outermost domain, which is

$$\hat{\phi}_l = \sum_{n,m} a_{nm,l} J_{n,l}^m + \sum_{n,m}\left(s_{nm,l} + rs_{nm,l}^{(\text{out})}\right) H_{n,l}^m. \tag{10}$$

The outermost potential field can also be split into two parts: the effective incident potential and

the effective scattering potential. However, comparing Eq. (10) with Eq. (8) shows that the results for the rescattering waves differ from those of the innermost domain where the rescattering waves play a role as incident waves, while they become another essential part of the scattering waves.

More generally, when the position vector $\vec{r}_l$ is located at the middle layers between the innermost and the outermost boundaries of the system $O_l$ (i.e., $R_{\text{in}} \le |\vec{r}_l| \le R_{\text{out}}$), for one of the source particles of $j$, some particles are located in the inner domain of $R_{\text{in}} \le |\vec{r}_l| \le |\vec{r}_{lj}|$ and others in the outer domain of $|\vec{r}_{lj}| \le |\vec{r}_l| \le R_{\text{out}}$, as illustrated in Fig. 2. The total scattering field cannot be completely formulated by either Eq. (7) or Eq. (9). Correspondingly, Eqs (8) and (10) become invalid for the middle layers. In order to further extend the theory, we start from Eq. (6) and the addition theorem to formulate the total scattering field with respect to the system $O_l$ as

$$\begin{aligned}\hat{\phi}_{\text{tsc},l} &= \sum_{n,m} s_{nm,l} H_{n,l}^m + \sum_{n,m}\left(\sum_{j\in\text{inner}}\sum_{\nu,\mu} s_{\nu\mu,j} S_{\nu,n}^{\mu,m\,(1)}\left(\vec{r}_{jl}\right)\right) H_{n,l}^m + \sum_{n,m}\left(\sum_{j\in\text{outer}}\sum_{\nu,\mu} s_{\nu\mu,j} S_{\nu,n}^{\mu,m\,(2)}\left(\vec{r}_{jl}\right)\right) J_{n,l}^m \\ &= \underbrace{\sum_{n,m} s_{nm,l} H_{n,l}^m}_{\hat{\phi}_{\text{sc},l}} + \underbrace{\sum_{n,m} rs_{nm,l}^{(\text{outer})} H_{n,l}^m + \sum_{n,m} rs_{nm,l}^{(\text{inner})} J_{n,l}^m}_{\hat{\phi}_{\text{rsc},l}},\end{aligned} \tag{11}$$

where symbols $j \in \text{inner}$ and $j \in \text{outer}$ represent the source particles involved in the inner domain and the outer domain, respectively. The outer rescattering coefficients are defined as $rs_{nm,l}^{(\text{outer})} \equiv \sum_{j\in\text{inner}}\sum_{\nu,\mu} s_{\nu\mu,j} S_{\nu,n}^{\mu,m\,(1)}\left(\vec{r}_{jl}\right)$, and likewise, the inner rescattering coefficients as $rs_{nm,l}^{(\text{inner})} \equiv \sum_{j\in\text{outer}}\sum_{\nu,\mu} s_{\nu\mu,j} S_{\nu,n}^{\mu,m\,(2)}\left(\vec{r}_{jl}\right)$. Correspondingly, the velocity potential function is

$$\begin{aligned}\hat{\phi}_l &= \sum_{n,m} a_{nm,l} J_{n,l}^m + \sum_{n,m} s_{nm,l} H_{n,l}^m + \sum_{n,m}\left(rs_{nm,l}^{(\text{outer})} H_{n,l}^m + rs_{nm,l}^{(\text{inner})} J_{n,l}^m\right) \\ &= \sum_{n,m}\left(a_{nm,l} + rs_{nm,l}^{(\text{inner})}\right) J_{n,l}^m + \sum_{n,m}\left(a_{nm,l} + rs_{nm,l}^{(\text{outer})}\right) H_{n,l}^m.\end{aligned} \tag{12}$$

Note that when $\text{inner}=\varnothing$, $rs_{nm,l}^{(\text{outer})} = 0$ and $rs_{nm,l}^{(\text{inner})} = rs_{nm,l}^{(\text{in})}$, which indicates that all position vector of source particles satisfy $|\vec{r}_l| \le R_{\text{in}} \le |\vec{r}_{lj}|$, Eq. (12) is consistent with Eq. (8). Similarly, when $\text{outer}=\varnothing$, $rs_{nm,l}^{(\text{outer})} = rs_{nm,l}^{(\text{out})}$, $rs_{nm,l}^{(\text{inner})} = 0$ and all source particles position vector satisfy

$\left|\vec{r}_{ij}\right| \le R_{\text{out}} \le \left|\vec{r}_{i}\right|$, Eq. (12) is compatible with Eq. (10).

As the acoustic pressure and velocity can be derived directly from the potential function, and the acoustic radiation force and the acoustic dissipation are directly related to the pressure and velocity, the force and the dissipation can be formulated under similar mathematical structures.

## 2.2. Acoustic attenuation along wave propagating direction

As the radiation forces are directly proportional to the square of the complex amplitude of pressure, namely the acoustic intensity, the acoustic energy distribution will be less or more different if the influence of the acoustic attenuation or acoustic energy dissipation becomes stronger or weaker. Interestingly, if the effects from the attenuation within the medium become strong enough, the incident wave behaves differently compared with no attenuation medium. One of the significant differences is that the stable points for particles will not be located at the nodes or the anti-nodes of the standing waves [4][11][31] but assemble at other position

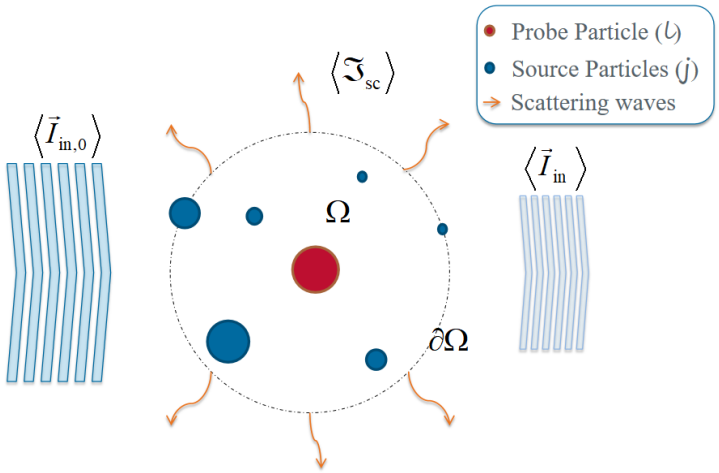


Fig. 3 The energy conservation and the definitions of spherical space $\Omega$ and scattering dissipation of the multiple particles environment.

Acoustic energy conservation is described by Eq. (A11) of Appendix II. Based on the relation, the

scattering dissipation $\Im_{\mathrm{sc}}$ is defined as the energy taken away by scattering waves from the incident wave interacting with the particles inside the spherical space $\Omega$, which can be described by the scattering potential $\phi_{\mathrm{sc}}$ as

$$\left\langle \Im_{\mathrm{sc}} \right\rangle = -\frac{\rho_0 \omega^2}{2c_0} \mathrm{Re}\left[ \int_{\partial\Omega} \hat{\phi}_{\mathrm{sc}} \cdot \hat{\phi}_{\mathrm{sc}}^{*} \mathrm{dS} \right], \tag{13}$$

where symbol $\mathrm{Re}$ means taking the real part of the expressions. $\hat{\phi}_{\mathrm{sc}}$ corresponds to the effective scattering potential function of the outermost domain, determined by Eq. (9). Then, inserting the effective scattering potential of Eq. (9) into Eq. (13), we arrive at

$$\left\langle \Im_{\mathrm{sc}} \right\rangle = \frac{\hat{p}_0^2}{2\rho_0 c_0} \frac{1}{k^2} \sum_{n,m} At_{nm,l} \cdot At_{nm,l}^{*}, \tag{14}$$

where $\hat{p}_0$ means the complex amplitude of acoustic pressure of external incident wave. The scattering dissipation coefficients $At_{nm,l} = s_{nm,l} + rs_{nm,l}^{(\mathrm{out})}$. It is worth noting that the scattering dissipation of the spherical space $\Omega$ does not involve any energy transformation, but that the acoustic energy of the incident wave is transferred into the scattering wave by reflection, thereby weakening the acoustic intensity in the incident direction.

The acoustic intensity along the direction of the incident wave $\vec{I}_{\mathrm{in}}$ and the attenuation coefficient $\alpha$ due to the scattering dissipation satisfy

$$\alpha \approx \left| \partial_x \left\langle \vec{I}_{in} \right\rangle \right| \Big/ (-2) \cdot \left| \left\langle \vec{I}_{in,0} \right\rangle \right|, \tag{15}$$

where $\partial_x \equiv \dfrac{\partial}{\partial x}$ and the initial value of the acoustic intensity $\left| \left\langle \vec{I}_{\mathrm{in},0} \right\rangle \right| = \dfrac{1}{2} \dfrac{\hat{p}_0^2}{\rho_0 c_0}$. Based on the energy relation and the assumption that the particles distribute homogeneously, the intensity attenuation per unit meter (along $x$ direction) and the scattering dissipation can be connected with the help of the space density factor $D_n$, which is defined as the number of the spherical

space $\Omega$ involved in the unit cubic meter space by

$$\left|\partial_x \left\langle \vec{I}_{\text{in}} \right\rangle\right| \approx -\left\langle \Im_{\text{sc}} \right\rangle \cdot D_n. \tag{16}$$

Using Eq. (15) and Eq. (16), the attenuation coefficient can be evaluated by the scattering dissipation and, more directly, by the effective scattering coefficients in the outermost domain using Eq. (14):

$$\alpha = \frac{D_n}{2k^2} \sum_{n,m} At_{nm,l} \cdot At^*_{nm,l}. \tag{17}$$

For simplification, the number and the initial distribution of the particles involved in the spherical space $\Omega$, as well as the value of the space density factor $D_n$ are decided by the volume concentration and the radii of the insoluble particles in the suspension under the premise that all particles are distributed homogeneously and uniformly.

It can be proved that sound attenuation from the relaxation processes due to heat transfer, viscosity, and evaporation is relatively small compared to the scattering dissipation. The former reaches its maximum when $\tau\omega = 1$ [46][47]. Regularly, for the small particles with radii ranging from 0.0 1 mm to 1 mm, the relaxation time $\tau$ varies from 0.001 s to 0.0001 s, which means the most effective frequencies are from 160 Hz to 1600 Hz. However, for ultrasonic scenarios, the frequencies are remarkably higher than the effective frequencies. Therefore, in this paper, we ignore the attenuation from these relaxation processes.

In addition, the acoustic streaming caused by nonlinear and attenuation effects in the host fluid is

negligible. Acoustic streaming may cause an additional drag force on the trapped particles. However, several experimental and theoretical studies showed that the acoustic streaming is less dominant for large particles [48][49]. In our range of interest, the radii of particles are comparable to the wavelength of operating frequency ( $r \sim \lambda$ ). We, therefore, ignore the effects of acoustic streaming.

## 2.3. Radiation interaction forces for the particles suspension

The acoustic radiation forces arising from the interaction between an external incident wave and a particle are evaluated as a surface integral of the velocity potential functions for the particle. The radiation forces act on the particle due to the scattering pressure that can be obtained [27]

$$\vec{F} = \int_{\mathrm{R}} \langle L \rangle \mathrm{d}\vec{\mathrm{A}}_{\mathrm{R}} - \rho_0 \int_{\mathrm{R}} \mathrm{d}\vec{\mathrm{A}}_{\mathrm{R}} \cdot \langle \vec{u}\vec{u} \rangle. \tag{18}$$

In the above equation, the angle brackets $\langle \cdot \rangle$ denote the time average of the variable therein, and $L$ is the acoustic Lagrange density defined as $L = \frac{1}{2}\rho_0 \vec{u} \cdot \vec{u} - \frac{1}{2\rho_0 c_0^2} p^2$, $\rho_0 \vec{u} \cdot \vec{u}$ is defined as the flux of momentum density, $\vec{u} = \vec{u}_{\mathrm{i}} + \vec{u}_{\mathrm{s}}$ is the acoustic velocity, and $p = p_{\mathrm{i}} + p_{\mathrm{s}}$ is the acoustic pressure with subscripts $\mathrm{i}$ and $\mathrm{s}$ for the incident and scattering waves, respectively. The spherical surface $\mathrm{R}$ surrounding the scattering particle is sufficiently far from the scattering source, and the direction of the integration element $\mathrm{d}\vec{\mathrm{A}}_{\mathrm{R}}$ is along the outer normal of the surface $\mathrm{R}$. To simplify Eq. (18), the following are considered. (i) For the external incident wave that does not contribute to the radiation force, i.e., $\int_{\mathrm{R}} \langle L_{\mathrm{i}} \rangle \mathrm{d}\vec{\mathrm{A}}_{\mathrm{R}} - \rho_0 \int_{\mathrm{R}} \mathrm{d}\vec{\mathrm{A}}_{\mathrm{R}} \cdot \langle \vec{u}_{\mathrm{i}}\vec{u}_{\mathrm{i}} \rangle = 0$, the acoustic Lagrange density for the incident wave is defined as $L_{\mathrm{i}} = \frac{1}{2}\rho_0 \vec{u}_{\mathrm{i}} \cdot \vec{u}_{\mathrm{i}} - \frac{1}{2\rho_0 c_0^2} p_{\mathrm{i}}^2$. (ii) the Sommerfeld radiation conditions require the acoustic Lagrange density for the scattering wave to satisfy $L_{\mathrm{s}} = \frac{1}{2}\rho_0 \vec{u}_{\mathrm{s}} \cdot \vec{u}_{\mathrm{s}} - \frac{1}{2\rho_0 c_0^2} p_{\mathrm{s}}^2 = 0$. Hence

$$\vec{F} = -\int_{\mathrm{R}} \frac{1}{c_0} \left[ \langle p_{\mathrm{i}}\vec{u}_{\mathrm{s}} \rangle + \langle p_{\mathrm{s}}\vec{u}_{\mathrm{s}} \rangle + \langle p_{\mathrm{s}}\vec{u}_{\mathrm{i}} \rangle \right] \mathrm{d}\vec{\mathrm{A}}_{\mathrm{R}}. \tag{19}$$

It is convenient to describe Eq. (19) by the velocity potential form as

$$\vec{F}=\int_{\mathrm{R}}\frac{\rho_0\omega^2}{c_0^2}\left[\left\langle\phi_{\mathrm{i}}\phi_{\mathrm{s}}\right\rangle\vec{e}_r+\left\langle\phi_{\mathrm{s}}\phi_{\mathrm{s}}\right\rangle+\left\langle\frac{\mathrm{i}c_0}{\omega}\phi_{\mathrm{s}}\nabla\phi_{\mathrm{s}}\right\rangle\right]\mathrm{d}\vec{\mathrm{A}}_{\mathrm{R}}, \tag{20}$$

where $\vec{e}_r$ is the unit outer normal vector of the spherical surface $\mathrm{R}$. The sum of terms makes two types of contributions, (i) squares of $\phi_{\mathrm{s}}$ representing the force from the scattering and rescattering waves, and (ii) the rest mixed terms representing the force from interference between the incoming and the scattered waves. Obviously, the radiation forces from Eq. (20) hold valid only for a single scatterer system, i.e., the problem of an external incident wave and the corresponding scattering wave. However, for the multi-particle system, based on Eq. (8) for the innermost domain, the velocity potential function $\phi_l$ can be split into the effective incident part and the effective scattering part. It means that, for probe particle in a multi-particle system, the radiation forces acting on the probe particle can be calculated by Eq. (20) using the potential function distribution of the innermost domain. The radiation forces calculation on the probe particle is reduced to that of the corresponding single-particle problem, as presented in a recent work [23].

The acoustic radiation forces on the probe particle with respect to the system $O_l$ can be evaluated under the Cartesian coordinate system by substituting Eq. (8) into Eq. (20), using relation $\left\langle XY\right\rangle=\frac{1}{2}\mathrm{Re}\left[\hat{X}\hat{Y}^*\right]$. Considering the orthogonality and the recurrence properties of the spherical harmonics function to simplify [45]:

$$\begin{cases} F_{x,l} = -\dfrac{\hat{p}_0^2}{4c_0^2\rho_0}\dfrac{1}{k^2}\mathrm{Re}[\mathrm{i}\cdot\sum_{n,m} b_{nm,l}(1+s_{n,l})(A_{n+1}^{m+1}bs_{n+1,m+1}^{*} - B_{n-1}^{m+1}bs_{n-1,m+1}^{*} + C_{n+1}^{m-1}bs_{n+1,m-1}^{*} - D_{n-1}^{m-1}bs_{n-1,m-1}^{*})] \\ F_{y,l} = +\dfrac{\hat{p}_0^2}{4c_0^2\rho_0}\dfrac{1}{k^2}\mathrm{Re}[\sum_{n,m} b_{nm,l}(1+s_{n,l})(A_{n+1}^{m+1}bs_{n+1,m+1}^{*} - B_{n-1}^{m+1}bs_{n-1,m+1}^{*} - C_{n+1}^{m-1}bs_{n+1,m-1}^{*} + D_{n-1}^{m-1}bs_{n-1,m-1}^{*})] \\ F_{z,l} = -\dfrac{\hat{p}_0^2}{2c_0^2\rho_0}\dfrac{1}{k^2}\mathrm{Re}[\mathrm{i}\cdot\sum_{n,m} b_{nm,l}(1+s_{n,l})(E_{n+1}^{m}bs_{n+1,m}^{*} - F_{n-1}^{m}bs_{n-1,m}^{*})] \end{cases} \quad (21)$$

where the combination coefficients $bs_{nm} \equiv b_{nm,l}s_{n,l}$, symbol $\mathrm{Re}$ means taking the real part of the expressions, superscript $*$ means conjugating the complex variables, $\hat{p}_0$ and $k$ mean the complex amplitude of acoustic pressure of external incident wave and the complex wavenumber for the multi-particle environment, respectively. The weighting coefficients $A_n^m$, $B_n^m$, $C_n^m$, $D_n^m$, $E_n^m$ and $F_n^m$ are defined as

$$A_n^m = -\sqrt{\frac{(n+m-1)(n+m)}{(2n-1)(2n+1)}}, B_n^m = \sqrt{\frac{(n-m+2)(n-m+1)}{(2n+1)(2n+3)}}, C_n^m = \sqrt{\frac{(n-m-1)(n-m)}{(2n-1)(2n+1)}}, \quad (22)$$
$$D_n^m = -\sqrt{\frac{(n+m+2)(n+m+1)}{(2n+1)(2n+3)}}, E_n^m = \sqrt{\frac{(n-m)(n+m)}{(2n-1)(2n+1)}}, F_n^m = \sqrt{\frac{(n-m+1)(n+m+1)}{(2n+1)(2n+3)}}.$$

Based on Eq. (21), the magnitude and the direction of the forces can be determined, which indicates that the particles will be moved along the direction of the forces.

Inserting Eq. (17) as the imaginary part of the complex wavenumber $k$ in Eq. (21), the acoustic radiation forces considering the dissipation by the scattering effects along the wave propagating direction are obtained.

# 3. Results and discussions

## 3.1. Example and calibration of theoretical pressure fields and attenuation coefficient

The prediction accuracies of the attenuation coefficient by Eq. (17) and the radiation forces by Eq. (21) depend on the potential field. Before further analyzing the results, the acoustic pressure field calculated by Eqs (8), (10), and (12) should be validated with that from simulations for the same geometry.

We have performed an acoustic scattering pressure field calculation for three rigid particles immersed in the air with two traveling waves along the $\pm z$ axes. The radii of the particles are 2 mm, located at (-8, 0, -8) mm, (0, 0, 0) mm and (8, 0, -8) mm, respectively. As the accuracy of the multiple scattering theory depends on accurately evaluating the scattered and rescattered fields, we intentionally selected particles with larger radii (the scattering effect is more significant if the particle radius is larger) to validate the accuracy between the theoretical and numerical results. The frequency, amplitude, and initial phase of incident waves are 40 kHz, 10 Pa, and 0 rad at the position (0, 0, 0) mm, respectively. The results are compared with finite element simulations using the COMSOL Multiphysics software. Specifically, the linear acoustic fields are modelled using the ‘Pressure Acoustics, Frequency Domain’ interface, the computational domain is enclosed by the ‘Perfectly Matched Layer’ to absorb all outgoing wave energy, and the particle surfaces are set

to the ‘Sound Hard Boundary’. The comparisons are illustrated in Fig. 4.

The theoretical predictions agree with full numerical simulations, with some amplitude deviations in the region far from the particles, which can be corrected by increasing the truncation number $M$. As a higher truncation number $M$ costs more computational time for the separation matrix $S_{\nu,n}^{\mu,m}\left(\vec{r}_{lq}\right)$, $M=12$ is chosen as a compromise.

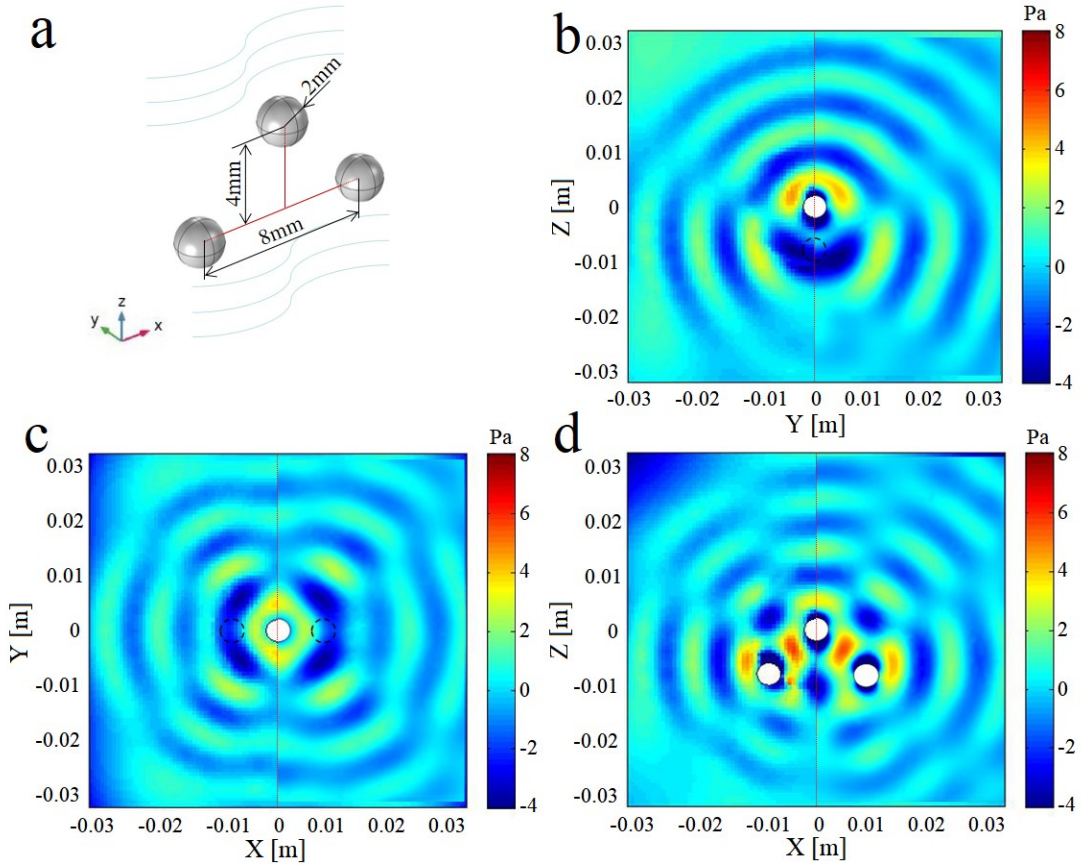


Fig. 4 The comparisons of the acoustic scattering pressure fields based on Eqs (8), (10), and (12) for the truncation number $M=12$ and those from the finite element simulations. **a** The geometric description of three rigid spherical particles in the air. The radii of the particles are all 2 mm, located at (-8, 0, -8) mm, (0, 0, 0) mm, and (8, 0, -8) mm, respectively, from the left-hand side to the right-hand side. **b, c, d** The acoustic scattering pressure fields source from two opposite

traveling waves interacting with these particles of the left view **b**, the vertical view **c,** and the front view **d**. The theoretical predictions based on Eqs (8), (10), and (12) are shown on the left-hand side, and the simulations are on the right-hand side separated by the red-dot lines in the middle of sub-figure **b, c, d**.

A plane wave attenuation is evaluated by Eq. (17) when the wave propagates through the suspension (insoluble particles immersed in water) with different volume concentrations and frequencies, as shown in Fig. 5. The diameter of the immersed particles is set as 32 μm (same with experiment [38]) with a rigid boundary condition. In order to summarize the results, the independent variable used to describe the attenuation coefficient is the size parameters (*ka*), not the particle radius (*a*) or frequency (*f*). Benefitting from the fact that the size parameter contains both particle size and frequency information [33][34][38], we use the size parameter as an independent variable to discuss the following.

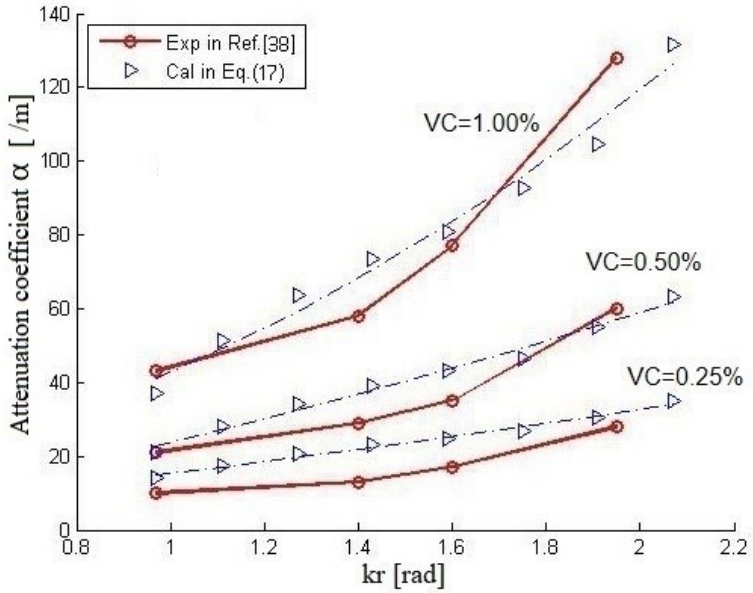

Fig. 5 Attenuation coefficient in the suspension based on Eq. (17) and experimental data with different suspension volume concentrations (VCs). The blue curves are quadratic polynomial fitting of theoretical results (the blue triangle symbols), and the red curves are experimental data of [38]

The theoretical calculation of the attenuation coefficient based on Eq. (17) is validated with experimental data of [34][38] (The red lines in Fig. 5). The operating frequency should satisfy $kr \geq 1$ so that the scattering dissipation plays a dominant role, while the effects caused by viscous dissipation can be safely neglected [34][37].

The frequency dependence of the attenuation coefficient $\alpha$ for the suspension is indicated in Fig. 5. It can be found that the trends and values of the attenuation coefficient $\alpha$ predicted by the models proposed in the current work are basically in good agreement with those from experiments. The perceivable discrepancies between predictions and experiments may arise from different settings in the boundary condition of the particles. The rigid boundary condition is applied in the predictions to simplify the calculations, while the droplets in the experiments are compressible.

### 3.2. The pressure field without acoustic attenuation inside the BAW device

The bulk acoustic wave (BAW) device [1] with four traveling waves or two orthogonal standing waves launched from four PZT transducers is used to verify the proposed theory. Specifically, the BAW device has two pairs of ultrasonic matched transducers. Each of the transducers consists of a PZT plate and a matching layer. The four manipulation transducers are designed to be acoustically matched with water. The absorbers in the backside of the PZT transducers are designed to absorb the extra acoustic energy. The diagrammatic sketch of the BAW device used in this study is illustrated in Fig. 6.

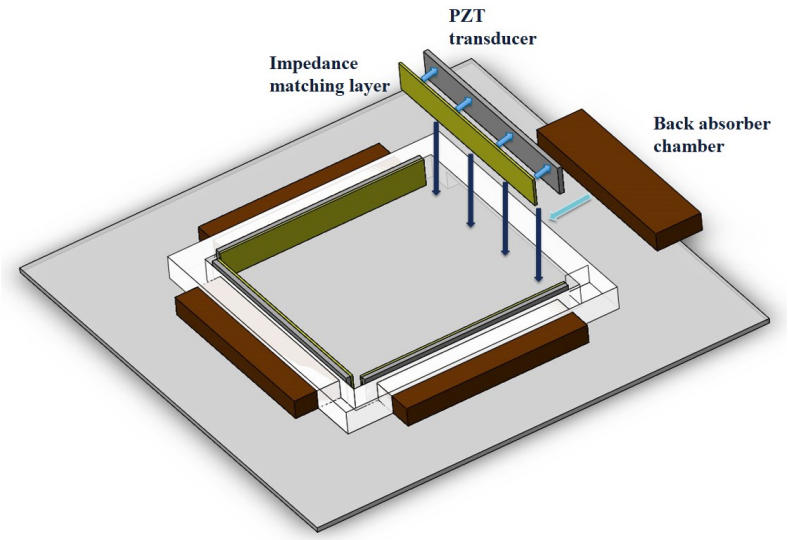


Fig. 6 The diagrammatic sketch of a square BAW device with the side lengths equal to 100 mm and the ultrasonic transducer includes an impedance matching layer in the front of a PZT plate and an absorbing layer in its back.

In order to reduce the reflection coefficient, the matching layer is designed to be a layer with a thickness that is an odd multiple of a quarter wavelength of incoming waves. For the PZT-5H material and the operating frequency of 600 kHz used in numerical simulations, the thickness of the matching layer (alumina-loaded epoxy [50]) is set as a quarter of the wavelength of incoming waves, 1.11 mm (with the speed of sound of 2670 m/s). As the resonance frequency is a function of the thickness of the PZT plate, there will be an optimal thickness for the excitation frequency of 600 kHz [1]. In this study, the thickness of the PZT plate is given as 3.2 mm. Overall, each transducer consists of a 100 mm length and 3.2 mm thick PZT plate with a 1.11 mm thick matching layer applied to the front face and an absorbing layer applied to the back face.

The detailed settings of the numerical simulation are described as follows: the BAW device mainly includes four domains; they are the central water-filled domain, four PZT plates, four matching layers, and four absorber chambers. The acoustic waves propagate in the water-filled domain, the matching layers, and the backing absorber chambers are modelled by the COMSOL 'Pressure Acoustics, Frequency Domain' interface. The PZT transducers are modelled by the 'Solid Mechanics' interface, applying the 'Piezoelectric Material' physics and 'PZT-5H' material. The acoustic absorption feature of the matching layers is modelled by setting the attenuation coefficient in the 'Alumina-loaded Epoxy' material; the attenuation coefficient and physical parameters are given in the experiments [50]. The absorber chambers, used to absorb the residual anti-propagated acoustic wave of the transducers, are defined as 'Perfectly Matched Layer'.

The pressure field resulting from the continuous sinusoidal excitation by all four transducers at

600 kHz is simulated with the same initial phase applied to each contribution. And the simulated result in the 100 × 100 mm region of the BAW device is shown in Fig. 7. For the excitation voltage used (50 Vpp), the maximum pressure reaches 550 kPa. In the region, the pressure varies sinusoidally with an amplitude of 550 kPa. There is a consistent pressure across most of the regions of interest, with some amplitude reduction and distortion near the sides [1][13][16][31].

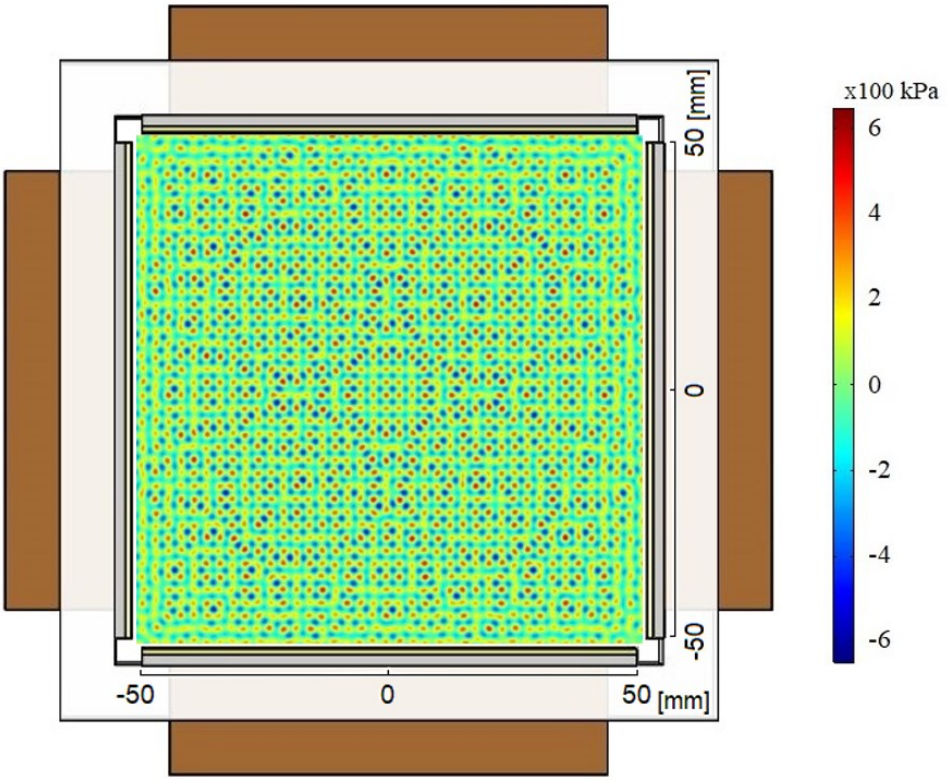


Fig. 7 Two-dimensional pressure field by simulation for the four transducer manipulation device excited at operating frequency 600 kHz and excitation voltage of 50 Vpp in the 100 x 100 mm region. The application of the initial phases of the four transducers are set as zeros.

### 3.3. Radiation force vectors in the BAW device with acoustic attenuation

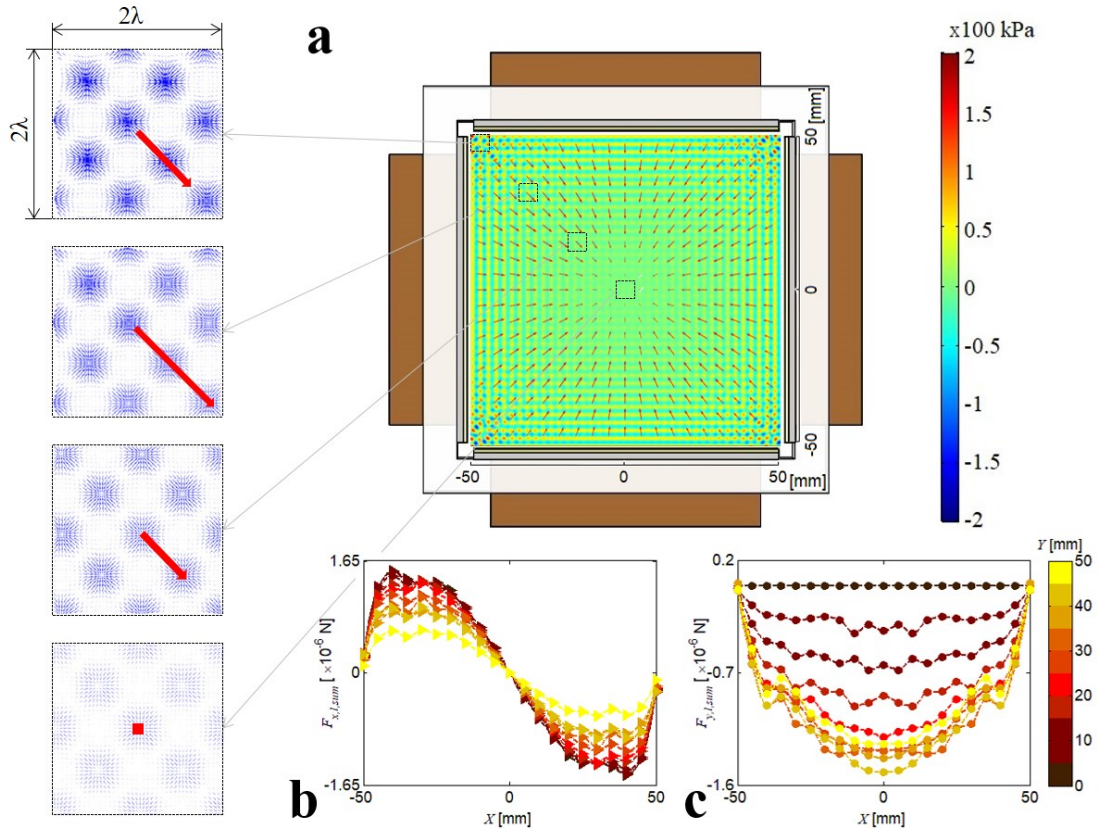


Fig. 8 **a** The force vectors and the pressure distribution from two orthogonal standing waves of 600kHz ( $kr \approx 1.3$ ) propagating through the suspension inside a square BAW device. The radiation force vectors are visualized with blue arrows, and a red arrow represents a resultant radiation force of a $2\lambda \times 2\lambda$ square lattice (i.e., $\vec{F}_{l,sum} = \sum_{inside\ lattice} \vec{F}_l$ ). Four expanded images, the centers of these squares located at coordinates of (45, 45) mm, (30, 30) mm, (15, 15) mm, and (0, 0) mm from the upper-left corner to the center of the computational domain, describe the radiation force vectors (blue arrows) directly from Eq. (21) and their corresponding resultant radiation force vectors (red arrows). The background pressure distribution is simulated by the corresponding numerical result under the BAW device. The attenuation coefficient

($\alpha = 45.5/\mathrm{m}$) used in simulation coming from experimental data of [34][38]. **b, c** Distributio n of X-component **b** and Y-component **c** of the resultant radiation forces along the cut lines of different Y-axis positions.

In this section, we have calculated the radiation forces in the BAW device described in Sec. 3.2 using Eq. (21). Two orthogonal standing waves with a frequency of 600 kHz and amplitude of 150 kPa are launched from the transducers, and the waves are propagating in the suspension with the volume concentration equal to 0.1. The radii of the immersed particles and the sound speed of water used in the calculation are 500 $\mu\mathrm{m}$ and 1480 m/s, respectively. Note that the acoustic energy taking away by the scattered and rescattered waves is modelled by an attenuation coefficient evaluated by Eq. (17), which is the imaginary part of the wavenumber in Eq. (21). In this way, the energy transfer due to the scattering effects of massive particles can be conveniently considered in the calculation of the acoustic radiation force.

The numerical model is consistent with that used in Sec. 3.2. However, as the number of suspended particles is huge, the coordinates of these massive particles are nearly impossible to specify, leading to direct numerical simulation impractically. As a result, we give an attenuation coefficient (based on experimental data) to simplify the numerical study. It is worth emphasizing that, in order to perform the numerical simulations, we need to input the known attenuation coefficient to the numerical model in advance, which is determined by experiments. By contrast, we provide a model to evaluate the attenuation coefficient in our theoretical model, which enables our method to evaluate the acoustic radiation force in massive particle suspensions without the

help of the experimental data.

The force vectors (Eq. (21)) within a square BAW device are shown in Fig. 8. As the wavelength of incident waves is much smaller than the size of the BAW device, it is difficult to obtain sufficient information by directly displaying the distribution of the radiation force vectors. In order to visualize the general features of the radiation forces, we separate the whole computational domain into $20\times 20$ square lattices, and the side lengths of each square lattice are $2\lambda$. Then, the radiation force vectors calculated inside the same square lattice are added together. A new resultant radiation force vector is created, which is used to represent the overall effect of these radiation forces. When the operating frequency satisfies $kr\approx 1.3$, the amplitude of incident waves will be attenuated due to the gradual scattering effects, and the scattering energies will be fully absorbed by predesigned surrounding sides of the BAW device. The magnitudes of the radiation force ($|\vec{F}|\sim|\hat{p}_0|^2$) will gradually reduce along these directions. Eventually, the force vectors are not directed in the directions of the nodes or anti-nodes, but clump into the central space, as shown in Fig. 8.

As the waves are significantly attenuated in the suspension by the scattering effects, the particles are more manipulated by the features of traveling waves than by the residual standing waves inside the domain. Compared with the pressure field of no attenuation scenario (Fig. 7), the amplitude of the pressure becomes weaker along the wave propagating directions, which indicates that the force vectors will point to the central space of the BAW device, where the pressure amplitude and the gradient of the pressure field tend to be smaller. Particles are trapped within this

region and eventually form an assembly (Fig. 8) instead of the well-known scaffold pattern [16][31]

From the sub-figure **b, c** of Fig. 8, the resultant radiation forces inside a $2\lambda \times 2\lambda$ square lattice are calculated to describe the overall effects of the forces acting on the particles. Generally, the magnitudes of forces increase with the distance to the central domain, and the forces point to the central domain. Specifically, the magnitudes of the resultant radiation forces reach the minimum value in the central domain, which indicates precisely that the particles can be trapped in this domain.

It is worth noting that the central assembly in the BAW device is not only suitable for particles of a specific diameter but can also be extended to particles of other sizes. We need to select an appropriate frequency ($kr \approx 1$) to ensure the scattering effects are significant enough. Based on this concept, the central assembly will become a tool to clump suspended particles or droplets together, increasing the possibility of particle interaction. Moreover, such a central pattern will be attractive for the chemical industry and research on droplet coalescence. Also, as the attenuation phenomenon is not significant for $kr \gg 1$, it is achievable to separate objects with different sizes and collect the target objects from one another.

## 4. Summary

We have presented a multiple-scattering theory, taking account of energy dissipation to calculate the acoustic velocity potential field in the multi-object environment. The potential field and the attenuation coefficient caused by the travelling wave dissipation based on the theory agree with numerical simulation and available experimental data. The theory is further applied to show the radiation force vectors in the BAW device, where a central assembling pattern can be found.

Different from the standard patterning method, which constrains the particles in the nodes and the anti-nodes resulting from the standing waves, a central assembly can be realized by introducing adequate energy dissipation for the traveling waves, forming a convergent wave field when travelling waves from opposite directions meet without significant reflection. The central assembly provides an option of contactless clumping of suspended objects, allowing droplets coalescence for rainfall, and even enhancing particle interaction. It may also allow contactless separation for objects with different sizes with an appropriate choice of frequency and spatial dimension. These and many other possibilities derived from this study will, we hope, benefit the chemical industry and beyond.

# Appendix I

The continuity of pressure and radial velocity across the boundary of the $i$ th particle (i.e., the balances of the potential field outside the particle calculating by Eq. (3) plus Eq. (7) with that inside the particle) gives

$$b_{nm,i} \cdot s_{n,i} = s_{nm,i}, \tag{A1}$$

where $b_{nm,i} = a_{nm,i} + rs_{nm,i}^{(\mathrm{in})}$ are the effective beam-shape coefficients of the system $O_i$, which can be regarded as a comprehensive effect of the external wave ( $a_{nm,i}$ ) and the rescattering waves from other particles interacting with $i$ th particle ( $rs_{nm,i}^{(\mathrm{in})}$ ). Equation (A1) indicates that solving the scattering coefficients $s_{nm,i}$ is equivalent to determining the effective beam-shape coefficients $b_{nm,i}$. The scalar scattering coefficients $s_{n,i}$ describe the scattering effect of the single-particle system, which is determined totally by the boundary condition on the surfaces between the $i$ th particle and the host fluid [30][43][44]. Specifically, for the inviscid compressible particl es considered here, the scalar scattering coefficients $s_{n,i}$ are expressed as

$$s_{n,i} = -\frac{\det\begin{bmatrix} \gamma_i j_n(ka_i) & j_n(k_i a_i) \\ j_n'(ka_i) & j_n'(k_i a_i) \end{bmatrix}}{\det\begin{bmatrix} \gamma h_n(ka_i) & j_n(k_i a_i) \\ h_n'(ka_i) & j_n'(k_i a_i) \end{bmatrix}}, \tag{A2}$$

where $k_i$ is the inner wavenumber of the $i$ th particle, $\gamma_i \equiv \dfrac{\rho_0 k_i}{\rho_i k}$, and the prime symbol indicates differentiation.

With the help of the definitions of the effective beam-shape coefficients $b_{nm,i}$ and the rescattering coefficients of the innermost domain $rs_{nm,l}^{(\mathrm{in})}$, we have

$$a_{nm,i} = b_{nm,i} - \sum_{j\neq l}^{N} \sum_{\nu,\mu} b_{\nu\mu,j} s_{\nu,j} S_{\nu,n}^{\mu,m(2)}\left(\vec{r}_{ji}\right). \tag{A3}$$

In the above equation, the beam-shape coefficients of different coordinate systems $a_{nm,i}$ and the scalar scattering coefficients for different particles $s_{n,i}$ are given in Eqs (4) and (A2), respectively. Therefore, Eq. (A3) immediately gives a set of $(M+1)^2 \times N$ equations, which can be solved for the unknown effective beam-shape coefficients $b_{nm,i}$ (i.e., the scattering coefficients $s_{nm,i}$). As the scattering coefficients $s_{nm,i}$ are found, the total scattering potential function $\phi_{\text{tsc}}$ in Eq. (6) is determined.

# Appendix II

A well-known energy conservation-dissipation corollary or acoustic energy conservation [40] is provided as

$$\frac{\partial w}{\partial t}+\nabla\cdot\vec{I}=-\Im'_{\mathrm{vis}}-\Im'_{\mathrm{T}}. \tag{A4}$$

In order to obtain the energy relation within a certain space, we define a spherical space $\Omega$. If the interaction effects from other source particles far from the probe particle can be ignored, the radius of that space is defined as five times larger as that of the probe particle.

As illustrated in Fig. 3, the integration of Eq. (A4) within this space $\Omega$ yields

$$\int_{\Omega}\frac{\partial w}{\partial t}\mathrm{dv}+\int_{\Omega}\nabla\cdot\vec{I}\,\mathrm{dv}=-\Im_{\mathrm{vis}}-\Im_{\mathrm{T}}, \tag{A5}$$

and

$$w=\frac{1}{2}\rho_0\vec{u}^2+\frac{1}{2}\frac{p^2}{\rho_0c_0^2}+\frac{1}{2}\left(\frac{\rho T}{c_{\mathrm{p}}}\right)_0 s^2, \tag{A6}$$

$$\vec{I}=p\vec{u}-\mu\vec{e}_j u_i\Phi_{ij}-\frac{\kappa}{T_0}T'\nabla T', \tag{A7}$$

$$\Im_{\mathrm{vis}}=\int_{\Omega}\Im'_{\mathrm{vis}}\mathrm{dv}=\int_{\Omega}\frac{1}{2}\mu\sum_{i=1}\sum_{j=1}\Phi_{ij}^2\mathrm{dv}, \tag{A8}$$

$$\Im_{\mathrm{T}}=\int_{\Omega}\Im'_{\mathrm{T}}\mathrm{dv}=\int_{\Omega}\frac{\kappa}{T_0}\left(\nabla T'\right)^2\mathrm{dv}. \tag{A9}$$

where variable $w$ and vector $\vec{I}$ mean the acoustic energy and the acoustic intensity, respectively. The variables describing the energy dissipation within the spherical space $\Omega$ include the viscous energy dissipation $\Im'_{\mathrm{vis}}$ and the thermal energy dissipation $\Im'_{\mathrm{T}}$. Moreover,

parameter $\kappa$ represents the thermal conductivity, parameter $\delta_{ij}$ is the Kronecker function, variable $\Phi_{ij} = \frac{\partial u_i}{\partial x_j} + \frac{\partial u_j}{\partial x_i} - \frac{2}{3}\nabla \cdot \vec{u}\delta_{ij}$ is defined as the rate-of-shear tensor, and other variables follow their common definitions.

Taking time-averaged of Eq. (A5) and ignoring the effect of heat transfer (i.e., $\Im'_{\mathrm{T}} = 0$), the acoustic energy conservation equation for space $\Omega$ can be rewritten as

$$\int_{\Omega} \nabla \cdot \langle \vec{I} \rangle \mathrm{dv} = -\langle \Im_{\mathrm{vis}} \rangle. \tag{A10}$$

Note that, theoretically and experimentally, the viscosity will play a dominant role in energy dissipation within the range of long-wavelength regime or Rayleigh regime ( $k_0 r \ll 1$ ) [34][37][38]. While for the Mie regime ( $k_0 r \approx \text{or} > 1$ ), the scattering dissipation becom es dominant (at least ten times more than the viscous dissipation [34][38]). As the magnitude of the radiation force is minimal for the Rayleigh regime compared with that for the Mie regime, the viscosity effect is ignored (i.e., $\Im_{\mathrm{vis}} \approx 0$ ) for the problems involved the Mie particles ( $k_0 r \sim \text{or} > 1$ ). On this Basis, the acoustic intensity in Eq. (A7) becomes $\vec{I} = p\vec{u}$ . Then, the acoustic energy equation Eq. (A10) can be simplified by means of the Gauss theorem as

$$\int_{\partial\Omega} \left\langle \phi \cdot \frac{\partial \phi}{\partial r} \right\rangle (-\mathrm{i}\rho_0 \omega) \mathrm{dS} = 0, \tag{A11}$$

where $\partial\Omega$ represents the boundary surface of the volume space $\Omega$, and $\phi$ is the velocity potential for the multi-particle environment. As the domain of integration belongs to the outermost domain (defined in Sec. 2.1), the velocity potential function can be physically separated into the effective incident potential function and the effective scattering potential function, i.e.,

$\phi = \phi_{\text{in}} + \phi_{\text{sc}}$ .

## Conflict of interest:

The authors declared that they have no conflicts of interest to this work.

# References


[1] C. R. P. Courtney, C.-K. Ong, B. W. Drinkwater, A. L. Bernassau, P. D. Wilcox, D. R. S. Cumming, Manipulation of particles in two dimensions using phase controllable ultrasonic standing waves, Proceedings of the Royal Society A: Mathematical, Physical and Engineering Sciences 468 (2011) 337.

[2] C. E. Owens, C. W. Shields, D. F. Cruz, P. Charbonneau, G. P. López, Highly parallel acoustic assembly of microparticles into well-ordered colloidal crystallites, Soft Matter 12 (2016) 717.

[3] B. W. Drinkwater, Dynamic-feld devices for the ultrasonic manipulation of microparticles, Lab on a Chip 16 (2016) 2360.

[4] J. P. K. Armstrong, S. A. Maynard, I. J. Pence, A. C. Franklin, B. W. Drinkwater, M. M. Stevens, Spatiotemporal quantifcation of acoustic cell patterning using voronoï tessellation, Lab on a Chip 19 (2019) 562.

[5] V. Vyas, M. Lemieux, D. A. Knecht, O. V. Kolosov, B. D. Huey, Micro-acoustic-trap (μat) for microparticle assembly in 3d, Ultrasonics sonochemistry 57 (2019) 193–202.

[6] A. Marzo, S. A. Seah, B. W. Drinkwater, D. R. Sahoo, B. Long, S. Subramanian, Holographic acoustic elements for manipulation of levitated objects, Nature communications 6 (2015) 8661.

[7] A. Marzo, M. Caleap, B. W. Drinkwater, Acoustic virtual vortices with tunable orbital angular momentum for trapping of mie particles, Physical review letters 120 (2018) 044301.

[8] Y. Niimura, K. Hasegawa, Evaporation of droplet in mid-air: Pure and binary droplets in single-axis acoustic levitator, PloS one 14 (2019) e0212074.

[9] A. Dolev, S. Davis, I. Bucher, Noncontact dynamic oscillations of acoustically levitated particles by parametric excitation, Physical Review Applied 12 (2019) 034031.

[10] G. Destgeer, B. H. Ha, J. H. Jung, H. J. Sung, Submicron separation of microspheres via travelling surface acoustic waves, Lab on a Chip 14 (2014) 4665.

[11] C. M. G. Atehortúa, N. Pérez, M. A. B. Andrade, L. O. V. Pereira, J. C. Adamowski, Water-in-oil emulsions separation using an ultrasonic standing wave coalescence chamber, Ultrasonics sonochemistry 57 (2019) 57.

[12] D. Foresti, K. T. Kroll, R. Amissah, F. Sillani, K. A. Homan, D. Poulikakos, J. A. Lewis, Acoustophoretic printing, Science advances 4 (2018) eaat1659.

[13] M. X. Lim, A. Souslov, V. Vitelli, H. M. Jaeger, Cluster formation by acoustic forces and active fluctuations in levitated granular matter, Nature Physics 15 (2019) 460.

[14] D. Foresti, M. Nabavi, M. Klingauf, A. Ferrari, D. Poulikakos, Acoustophoretic contactless transport and handling of matter in air, Proceedings of the National Academy of Sciences 110 (2013) 12549–12554.

[15] Y.-X. Shen, Y.-G. Peng, F. Cai, K. Huang, D.-G. Zhao, C.-W. Qiu, H. Zheng, X.-F. Zhu, Ultrasonic super-oscillation wavepackets with an acoustic meta-lens, Nature communications 10 (2019) 3411.

[16] C. D. Wood, J. E. Cunningham, R. O'Rorke, C. Wälti, E. H. Linfeld, A. G. Davies, S. D. Evans, Formation and manipulation of two-dimensional arrays of micron-scale particles in microfluidic systems by surface acoustic waves, Applied Physics Letters 94 (2009) 054101.

[17] L. Rayleigh, On the circulation of air observed in kundt's tubes, and on some allied acoustical problems, Philosophical Transactions of the Royal Society of London 175 (1884) 1.

[18] L. Rayleigh, On the momentum and pressure of gaseous vibrations, and on the connection with the virial theorem, Phil. Mag. 3 (1902) 338–346.

[19] L. V. King, On the acoustic radiation pressure on spheres, Proceedings of the Royal Society of London. Series A-Mathematical and Physical Sciences 147 (1934) 212–240.

[20] K. Yosioka, Y. Kawasima, Acoustic radiation pressure on a compressible sphere, Acta Acustica United with Acustica 5 (1955) 167–173.

[21] T. Hasegawa, K. Yosioka, Acoustic-radiation force on a solid elastic sphere, The Journal of the Acoustical Society of America 46 (1969) 1139–1143.

[22] L. P. Gor'kov, On the forces acting on a small particle in an acoustical feld in an ideal fluid, in: Sov. Phys. Dokl., Vol. 6, 1962, p. 773.

[23] J. H. Lopes, M. Azarpeyvand, G. T. Silva, Acoustic interaction forces and torques acting on suspended spheres in an ideal fluid, IEEE Trans. Ultrason. Ferroelectr. Freq. Control 63 (2016) 186.

[24] E. G. Williams, Fourier acoustics: sound radiation and nearfeld acoustical holography, Elsevier, 1999.

[25] P. A. Martin, Multiple scattering: interaction of time-harmonic waves with N obstacles, Cambridge University Press, 2006.

[26] Z. Liu, C. T. Chan, P. Sheng, A. L. Goertzen, J. H. Page, Elastic wave scattering by periodic structures of spherical objects: Theory and experiment, Physical Review B 62 (2000) 2446.

[27] P. J. Westervelt, The theory of steady forces caused by sound waves, The Journal of the

Acoustical Society of America 23 (1951) 312.

[28] P. J. Westervelt, Acoustic radiation pressure, The Journal of the Acoustical Society of America 29 (1957) 26.

[29] G. T. Silva, An expression for the radiation force exerted by an acoustic beam with arbitrary wavefront (l), The Journal of the Acoustical Society of America 130 (2011) 3541–3544.

[30] G. T. Silva, Off-axis scattering of an ultrasound bessel beam by a sphere, IEEE transactions on ultrasonics, ferroelectrics, and frequency control 58 (2) (2011) 298–304.

[31] G. T. Silva, J. H. Lopes, J. P. Leão-Neto, M. K. Nichols, B. W. Drinkwater, Particle patterning by ultrasonic standing waves in a rectangular cavity, Physical Review Applied 11 (2019) 054044.

[32] C. J. T. Sewell, The extinction of sound in a viscous atmosphere by small obstacles of cylindrical and spherical form, Proceedings of the Royal Society of London. Series A, Containing Papers of a Mathematical and Physical Character 83 (1910) 547.

[33] P. S. Epstein, R. R. Carhart, The absorption of sound in suspensions and emulsions. i. water fog in air, The Journal of the Acoustical Society of America 25 (1953) 553.

[34] J. R. Allegra, S. A. Hawley, Attenuation of sound in suspensions and emulsions: Theory and experiments, The Journal of the Acoustical Society of America 51 (1972) 1545–1564.

[35] B. Mascaro, T. Brunet, O. Poncelet, C. Aristégui, S. Raffy, O. Mondain-Monval, J. Leng, Impact of polydispersity on multipolar resonant scattering in emulsions, The Journal of the Acoustical Society of America 133 (2013) 1996–2003.

[36] D. J. McClements, Comparison of multiple scattering theories with experimental measurements in emulsions, The Journal of the Acoustical Society of America 91 (1992) 849.

[37] M. S. Greenwood, J. L. Mai, M. S. Good, Attenuation measurements of ultrasound in a kaolin–water slurry: a linear dependence upon frequency, The Journal of the Acoustical Society of America 94 (1993) 908.

[38] V. J. Stakutis, R. W. Morse, M. Dill, R. T. Beyer, Attenuation of ultrasound in aqueous suspensions, The Journal of the Acoustical Society of America 27 (1955) 539.

[39] V. Leroy, A. Strybulevych, J. H. Page, M. G. Scanlon, Sound velocity and attenuation in bubbly gels measured by transmission experiments, The Journal of the Acoustical Society of America 123 (2008) 1931.

[40] A. D. Pierce, R. T. Beyer, Acoustics: An introduction to its physical principles and applications. 1989 Edition, Acoustical Society of America, 1990.

[41] N. Fang, D. Xi, J. Xu, M. Ambati, W. Srituravanich, C. Sun, X. Zhang, Ultrasonic metamaterials with negative modulus, Nature materials 5 (2006) 452.

[42] X. Zhou, G. Hu, Acoustic wave transparency for a multilayered sphere with acoustic metamaterials, Physical Review E 75 (2007) 046606.

[43] G. T. Silva, Acoustic radiation force and torque on an absorbing compressible particle in an inviscid fluid, The Journal of the Acoustical Society of America 136 (5) (2014) 2405–2413.

[44] J. Leão-Neto, G. T. Silva, Acoustic radiation force and torque exerted on a small viscoelastic particle in an ideal fluid, Ultrasonics 71 (2016) 1–11.

[45] G. B. Arfken, H. J. Weber, Mathematical methods for physicists, American Association of Physics Teachers, 1999.

[46] F. E. Marble, Some gasdynamic problems in the flow of condensing vapors, Astronautica Acta 14 (1969) 585–613.

[47] G. Davidson, Sound propagation in fogs, Journal of the Atmospheric Sciences 32 (1975) 2201–2205.

[48] S. M. Hagsäter, T. G. Jensen, H. Bruus, J. P. Kutter, Acoustic resonances in microfluidic chips: full-image micro-piv experiments and numerical simulations, Lab on a Chip 7 (2007) 1336–1344.

[49] N. R. Skov, J. S. Bach, B. G. Winckelmann, H. Bruus, 3d modeling of acoustofluidics in a liquid-flled cavity including streaming, viscous boundary layers, surrounding solids, and a piezoelectric transducer, Aims Mathematics 4 (2019) 99–111.

[50] H. Wang, T. Ritter, W. Cao, K. K. Shung, High frequency properties of passive materials for ultrasonic transducers, IEEE transactions on ultrasonics, ferroelectrics, and frequency control 48 (2001) 78–84.